Machine learning accelerated discovery of corrosion-resistant high-entropy alloys

Cheng Zeng[*,‡], Andrew Neils, Jack Lesko, Nathan Post[*]

The Roux Institute, Northeastern University, Portland, Maine, 04101, United States.
[‡] *The Experiential AI Institute, Northeastern University, Boston, Massachusetts, 02115, United States*
[*] *Corresponding authors: Email: c.zeng@northeastern.edu and n.post@northeastern.edu, Tel: +1 401-396-6668 and +1 781-605-8671*

September 28, 2023

Abstract

Corrosion has a wide impact on society, causing catastrophic damage to structurally engineered components. An emerging class of corrosion-resistant materials are high-entropy alloys. However, high-entropy alloys live in high-dimensional composition and configuration space, making materials designs via experimental trial-and-error or brute-force ab initio calculations almost impossible. Here we develop a physics-informed machine-learning framework to identify corrosion-resistant high-entropy alloys. Three metrics are used to evaluate the corrosion resistance, including single-phase formability, surface energy and Pilling-Bedworth ratios. We used random forest models to predict the single-phase formability, trained on an experimental dataset. Machine learning inter-atomic potentials were employed to calculate surface energies and Pilling-Bedworth ratios, which are trained on first-principles data fast sampled using embedded atom models. A combination of random forest models and high-fidelity machine learning potentials represents the first of its kind to relate chemical compositions to corrosion resistance of high-entropy alloys, paving the way for automatic design of materials with superior corrosion protection. This framework was demonstrated on AlCrFeCoNi high-entropy alloys and we identified composition regions with high corrosion resistance. Machine learning predicted lattice constants and surface energies are consistent with values by first-principles calculations. The predicted single-phase formability and corrosion-resistant compositions of AlCrFeCoNi agree well with experiments. This framework is general in its application and applicable to other materials, enabling high-throughput screening of material candidates and potentially reducing the turnaround time for integrated computational materials engineering.

Graphical abstract:
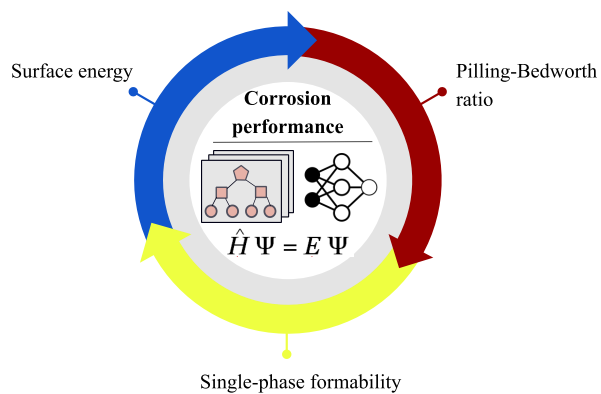
1 Introduction

High-entropy alloys are generally defined as alloys comprising no less than four elements and the percentage of each principal element is between 5 at.% and 35 at.%. The high-entropy concept was coined by Cantor [1] and Yeh [2] for equiatomic alloys with no less than five elements in 2004 almost the same time. The definition has been slightly extended to non-equimolar alloys with no less than four principal elements. This new class of materials has attracted increasing attention, found to display superior materials performance for mechanical properties [3–7], radiation resistance [8, 9] and corrosion resistance [10–12]. The high entropy of mixing usually leads to the formation of a disordered single phase for high-entropy alloys, such as face-centered cubic (FCC), body-centered cubic (BCC) and hexagonal closely-packed structures (HCP) [13, 14]. The homogeneous single phase improves passivity. In addition, high-entropy alloys can consist of elements with high passivation potency such as nickel, chromium, aluminum and titanium, leading to high pitting corrosion resistance.

Conventional corrosion-resistant alloys are mostly found by serendipity. Advances in physical theories, computational hardware and algorithms allow for rapid screening of candidate materials, paving the way for integrated computational materials engineering which aims to demystify the linkage between process, structure, property and performance. However, computational screening of corrosion-resistant alloys is challenging in that many factors can influence corrosion performance, including environmental conditions, chemical compositions and microstructures. Moreover, fundamental understanding of corrosion and various corrosion types adds more complexity to the material design. Recent works have been focused on building reliable databases for corrosion informatics, identifying reliable descriptors for corrosion performance and understanding the corrosion kinetics with multi-physics simulations [15–17]. Nyby et al. compiled a database for four types of alloys with an emphasis on six metrics used to describe their localized pitting corrosion [16]. Diao et al. collected a dataset for low-alloy steel and built machine learning models to predict their corrosion rate [18]. Roy et al. used machine learning algorithms to select the top three descriptors for prediction of the corrosion rates, including pH of the medium, halide concentration and composition of elements with the minimum reduction potential [19]. Taylor et al. identified a number of corrosion descriptors, such as cohesive energies, oxide formation energies and surface enrichment of passive elements, and related those descriptors to corrosion resistance with respect to surface passivation, dissolution and microstructure control [15]. Ke and Taylor reviewed the role of density functional theory (DFT) in modeling corrosion, and they pointed out corrosion metrics accessible by DFT, including oxygen and chloride adsorption energy, dissolution potential and surface energy [20]. Other computational methods based on peridynamics and phase-field modeling are often used to study the evolution of pitting corrosion [17, 21].

Unfortunately, the complexity of corrosion process makes it almost impossible to relate chemical compositions and microstructures of alloys directly to the corrosion performance. The vast composition and microstructure space of high-entropy alloys create complexity for the materials design problem. A workaround is multi-objective optimization based on empirical rules, which allows for screening material candidates with relative superior corrosion resistance. While some data-driven approaches and first-principles calculations exist to identify corrosion descriptors, those data-driven methods in nature lack physical insights and first-principles calculations are costly computationally. A physically meaningful and efficient approach to relating compositions with corrosion performance is still lacking.

The objective of this work is to bridge the technical gap for locating high-entropy alloys with potential high corrosion resistance in the high-dimensional composition space, in particular for pitting corrosion. We focused on pitting corrosion because the rate of localized pitting corrosion can be faster than uniform corrosion by orders of magnitude, hence pitting corrosion is more critical in applications where it exists [16]. A complete picture of pitting corrosion requires multi-scale and multi-physics simulations to understand the formation of passive film, passive film breakdown and pit growth stability [22], which to the best of our knowledge are not available. Pitting corrosion resistance is empirically associated with the ability of alloys to form a passive film, protectiveness of the passive film and pitting growth rate when the passive film breaks down. In this work, we chose three corrosion metrics considered to be influential to pitting corrosion, including *single phase formability*, *Pilling-Bedworth ratio* of passive elements, *surface energy*. A physics-informed machine learning (ML) framework was introduced to quantify the three corrosion metrics for a wide range of compositions of high-entropy alloys. The compositions with desired corrosion performances were identified by mapping out those corrosion metrics as a function of compositions. We tested this framework for AlCrFeCoNi high-entropy alloys because they belong to an emerging class of materials with superior mechanical properties and corrosion resistance [10, 23].

2   Theories and Methods

The aim of this work is to develop machine learning methods to quantify three metrics dictating pitting corrosion resistance of high-entropy alloys. The inputs of the machine learning models are the chemical compositions and the outputs are the corrosion metric. Random forest classification models trained on experimental data were used to decide whether a single phase is likely to form or not for a given chemical composition, whereas machine learning potentials trained on first-principles data were employed to calculate Pilling-Bedworth ratios and surface energies. In this section, we discuss in detail the qualitative relationship of the three metrics with pitting corrosion resistance and how to quantify each of them by machine learning models. The overall workflow of how to train the machine learning models is illustrated in Figure 1.

2.1   Single phase formability

The single phase formability was evaluated by a random forest classification model, also known as random forest classifier. It is crucial to form a homogeneous single phase for enhanced corrosion protection because it enhances passivity and prevents the fast galvanic corrosion. A physically rigorous approach to model single phase formation is thermodynamic modeling carried out with CALPHAD. The reliability of CALPHAD calculations is determined by the quality of experimental data as well as relevant first-principles calculations [24]. Instead of thermodynamic modeling, we used random forest models trained on experimental data to predict the probability of forming single phases for an arbitrary alloy composition. The experimental dataset was summarized by Yan et al. [25]. The workflow for single phase formability is shown in the top row of Figure 1. The raw data in total has 1807 entries and it takes input as the chemical compositions and output as the indicator for single phase formability. Single-phase alloys are labeled as '1', whereas multiple-phase alloys are labeled as '0'. It should be noted that phase formations are also dependent on the manufacturing processes and thermal history. It is assumed that most alloys found in this
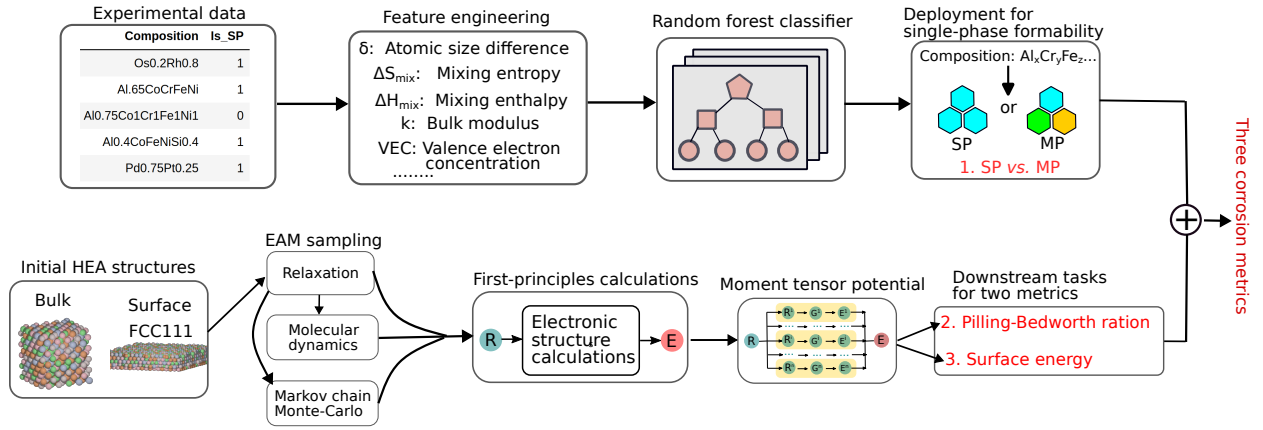
Figure 1: Workflow of machine learning accelerated discovery of corrosion-resistant high-entropy alloys.

experimental dataset were processed with similar techniques and environmental conditions, and the remaining exceptions represent outliers and noise in the dataset, whose impact on the robustness of ML models will be diminished by a cross-validation strategy due to the averaging effect. Each input composition was converted to eight physical descriptors, as used by Yan et al [25], including atomic size difference, mixing enthalpy, mixing entropy, Pauli electronegativity difference, molar volume, bulk modulus, melting temperature and valence electron concentration. Next, random forest models were trained to relate the eight descriptors to the single phase formability. The trained random forest models are thus able to predict if alloys will form single phase or multiple phases for a given composition. For the purpose of model validation, we held out 20% of the entire dataset for testing, which were used to examine the prediction accuracy of the final model on some unseen dataset, hence avoiding overfitting. Five-fold cross-validation was used on the remaining 80% dataset to tune the hyperparameters and to train the random forest classifier. The entire dataset was shuffled before splitting with a given random state to a test set and a data set for cross-validation, and ten random states were used to estimate uncertainties due to data splitting. Details of each descriptor, exploratory data analysis (Figure S1-S3), and hyperparameters of random forest models are included in the supporting information (SI).

2.2 Pilling-Bedworth ratio

The Pilling-Bedworth ratios and surface energies were quantified by machine learning potentials, which are trained following the procedure outlined in the bottom row of Figure 1. Pilling-Bedworth ratio (PBR) was used to describe the growth stress of an oxidation process. It describes the volume change due to oxidation on an alloy surface, which follows Eq. (1) with respect to the oxidation of a metallic element B.

$$PBR_{\mathrm{B}} = \frac{\text{Volume of a mole of } B_xO_y}{\text{Volume of x moles of B in metal}} \tag{1}$$

It is well accepted that when $PBR < 1$, the formed oxide offers no protection to the alloy surface. If $1 \leq PBR \leq 2$, the oxide forms a passive layer and prevents structural alloys from direct corrosion although some compression stresses develop inside the oxide. When $PBR \gg 2$,

the compression stresses become significant, causing the breakdown of the oxides. This simple analysis well explains that corrosion-resistant alloys typically contain Al, Zr, Ni, Ti, Fe or Cr whose PBR values are larger than 1 and not much larger than 2 [12, 26, 27].

When it comes to the oxidation of alloys, one or more elements may oxidize and form passive layers. Hence we need to identify elements that are thermodynamically preferential for oxidation. We can then calculate the PBR of the identified passive element by analyzing the volume change due to its oxidation. Xu and Gao introduced methods to compute PBR for the oxidation of alloys [28]. There are two possible cases for PBR values of alloys, depending on the relative diffusion rate of the passive element in alloys versus that in oxides. Generally the diffusion rate of passive elements within alloys are much faster relative to the rate within oxides so that alloy compositions near the surface can maintain a stoichiometry close to the original composition. For example, the diffusion coefficient of Cr in CrCrFeMnNi high-entropy alloys at 900 °C is about 10^{-12} cm^2/s while self-diffusion of Cr in Cr$_2$O$_3$ has a coefficient on the order of 10^{-21} to 10^{-17} cm^2/s [29, 30]. We recommend that readers consult the work of Xu and Gao [28] for calculation details of PBR for oxidation of alloys. For our benchmark material system AlCrFeCoNi, we examined the passivation of the Cr element although thermodynamic data, as tabulated in the SI, favors the formation of Al oxides over Cr oxides. Experimental data suggest that the addition of Al in CrFeCoNi alloys reduces passive film protection, implying that the major protection against pitting corrosion might be offered by the passivation of Cr [31]. Therefore, we consider the oxidation of Cr, which forms Cr$_2$O$_3$ with a mole weight of 102 g/mol and a density of 5.22 g/cm^3. The volume of Cr in the alloy was calculated using a FCC crystal whose lattice parameters were obtained by machine learning potentials.

2.3 Surface energy

The role of crystallographic orientation and the corresponding surface energy in corrosion protection was first investigated by Song et al [32]. It is found that a densely packed surface with a lower surface energy could lead to a stronger bonding between surface atoms that impedes the dissolution of surface atoms to solutions. The electrochemical dissolution rate I_A of a metal 'A' with an exposed crystal plane (h,k,l) at a temperature T follows the relation:

$$I_{A,(h,k,l)} \propto \exp\left(\frac{\alpha\gamma_{(h,k,l)}}{RT}\right) \tag{2}$$

where R is the gas constant, $\gamma_{(h,k,l)}$ is the surface energy and α is a transition coefficient to relate surface energy to dissolution activation energy. Ramachandran and Nosonovsky found that a lower surface energy leads to a more hydrophobic surface, and hydrophobic surfaces tend to show higher corrosion resistance [33]. In this work, we used surface energy as a metric to describe the trend of average dissolution of atoms on the crystallographic plane FCC(111) of AlCrFeCoNi alloys with different compositions. An FCC(111) facet wast used because of its high stability over other types of facets. It is arguable that a higher surface energy is associated with a higher average dissolution rate, resulting in faster pitting growth, although a more rigorous treatment may need to take into account sequential atom-by-atom dissolution on a metallic surface constrained by broken passive films formed on top of it, which we elected not to consider for the sake of simplicity. Surface energy of a facet reads as:

$$\gamma = \frac{E_{\text{slab}} - E_{\text{bulk}}}{2A} \tag{3}$$

where E_{slab} and E_{bulk} are respective potential energies of the FCC(111) facet and bulk cell, and A is the exposed area of the facet. The bulk cells used to calculate surface energies are of $L1_2$ structures, and the surface structures are the putative most stable structures found by Markov chain Monte-Carlo (MCMC) simulations. All items in Eq. 3 were found by atomistic modeling using machine learning potentials. The details of MCMC simulations are provided in the SI.

2.4 Machine learning potentials

Potential energy surfaces (PESs) represent one-to-one mappings between atomic positions ($\{R\}$) and potential energy (E) of a material system. PESs provide a plethora of information for material systems. For example, local minima on PESs represent stable states and the minimum energy trajectory connecting two local minima indicates a fundamental reaction pathway. The most often used methods to build reliable PESs are DFT calculations. However, standard DFT calculations are limited to hundreds of atoms due to the formidable $\mathcal{O}(M^{2-3})$ scaling with system sizes (M), such as numbers of basis sets, atoms or electrons [34]. It is thus computationally prohibitive to sample all points on *ab initio* PESs. One should note that DFT, first-principles and *ab initio* calculations are used interchangeably as they have the same meaning in this work. In the past decade, fitting *ab initio* PESs with machine learning (ML) algorithms have gained increasing momentum, and the ML-fitted PESs are termed machine learning potentials (MLP). Most MLPs relies on the nearsightedness principles [35], also known as *all chemistry is local*, implying that the total potential energy of a system with N atoms can be largely decomposed into a linear sum of all atomic contributions and each atomic contribution comes from the atom i interacting with neighboring atoms in a cutoff region, written as Eq. 4.

$$E = E(\{R\}) = \sum_{i=1}^{N} E_i = \sum_{i=1}^{N} E_i^{(\text{local})} \tag{4}$$

Thanks to and only because of the nearsightedness principle, MLPs can be trained with small-size first-principles data while allowing for reliable predictions on much larger systems [36]. It should be noted that the nearsightedness of first-principles calculations and machine learning algorithms should be well aligned to strike a good balance between computational efficiency and prediction accuracy [37]. A variety of ML algorithms have proven effective in fitting *ab initio* PESs, such as neural networks [36, 38], Gaussian process [39] and kernel ridge regression [40]. MLPs find applications in many fields, ranging from small molecules, to nanoparticle alloy catalysts and extended systems [41–43]. In this work, we employed a class of machine learning potentials termed moment tensor potentials (MTPs) for the high-entropy alloys which were found to be superior to other types of MLPs when tested on single-element systems by various simulation tasks [44]. Readers should refer to the work of Shapeev for implementation details of MTPs [45, 46]. MTPs were trained with systematically generated training data for high-entropy alloys AlCrFeCoNi, as outlined in the bottom row of Figure 1. We primed the algorithm with FCC bulk and surface structures. For each of the initial structures, atomic positions and lattice geometry are simultaneously optimized to find the stable structure, the process of which is termed structure optimization, also

known as relaxation. The structure optimization used the embedded atom method (EAM) developed by Farkas and Caro [47]. Starting with relaxed structures and using EAM, we also sampled a diverse pool of atomic configurations via molecular dynamics and Monte-Carlo simulations. The molecular dynamics simulations were used to perturb atomic positions, whereas the Monte-Carlo simulations were adopted to simulate exchange of two different atoms. Electronic structure calculations with GPAW were performed to refine the energy and forces of a part of the EAM-sampled configurations [48]. Additionally, we carried out first-principles calculations for simple bulk and surface structures with numbers of elements ranging from one to five. Special quasi-random structures were generated using the tool in the alloy theoretic automated toolkit (ATAT) for simple bulk structures with more than two elements to best approximate a random solid solution [49, 50]. In total, 1569 first-principles structures were curated. We then trained MTPs upon those data, and we used the MTPs to carry out simulations needed to calculate PBRs for the oxidation of Cr and surface energies of FCC(111) facets. Atomic structures were created and manipulated with the Atomic Simulation Environment (ASE) [51] and LAMMPS [52]. Computational settings of MTPs and GPAW calculations and details of the training data can be found in the SI. MTP enabled simulations to calculate relevant corrosion metrics are also elaborated in the SI. Scripts and notebooks for atomistic modeling and curation of training data will be supplied as a supporting dataset.

2.5 Mapping corrosion metrics with respect to Al and Cr compositions in AlCrFeCoNi

We tested the above methods on predicting the three corrosion metrics for AlCrFeCoNi high-entropy alloys. We varied the compositions of Al and Cr while equalizing remaining Fe, Co and Ni compositions. For a given composition, its single-phase formability was calculated by a random forest classifier and its Pilling-Bedworth ratio and surface energy were quantified by the MTPs. Therefore, we mapped the three corrosion metrics as a function of AlCrFeCoNi compositions, based on which we can identify composition regions with desired values for all corrosion metrics, which are potentially associated with superior relative corrosion resistance. We changed Al compositions in the range of 0–25 at.%, and Cr compositions in the range of 10–30 at.% (see Figure 3). The lower bound for the Cr composition was set as 10% because Cr is the passive element, and a percolation model for passivation of alloys suggests that the smallest amount of elements to enable passivation is around 10% [53]. In other words, an alloy only forms a continuous and protective passive film with the passive element being of no less than 10 at.%. For single-phase formability, an interval of 1% was used for both Al and Cr composition mesh grids as the inference by the trained random forest classifier for each composition took less than 1 second. For PBR_{Cr}, an interval of 5% was used to find the lattice parameters of $L1_2$ bulk cells using MTPs. The lattice parameters of MTP-relaxed structures were then fitted by a linear regression as a function of Al and Cr compositions. The fitted function was used to calculate lattice parameters for arbitrary Al and Cr compositions. The volume of Cr will be used to calculate PBR_{Cr}. In terms of surface energies, a composition interval of 5% was used to generate structures needed.

Table 1: Lattice constants and FCC(111) surface energies for single-element structures: DFT *versus* MTP.

	Lattice constant [Å]		Surface energy [J/m^2]	
Element	MTP	DFT	MTP	DFT
Al	4.08	4.04	0.77	0.86
Cr	3.62	3.62	2.61	2.65
Fe	3.44	3.46	2.49	2.45
Co	3.49	3.46	1.87	2.12
Ni	3.51	3.52	1.93	2.14

3 Results and discussion

3.1 ML prediction accuracy and transferability

ML models are often criticized for their poor transferability to data that are not existent in the training data set. As a result, it is of great importance to evaluate ML model performance before we deploy the models.

3.1.1 Random forest classifier

The experimental dataset used to train the random forest classifier includes in total 1807 entries. The 1807 data points were split to 80% and 20% for cross-validation and test, respectively. Hence 361 data points were used for testing, and ten different random states for the data splitting were used to obtain the standard deviation of model prediction accuracy on the test set. The random forest classifier gave a prediction accuracy of 89% on the test set with a standard deviation of 1%. The best model with the highest accuracy on the test set was chosen for subsequent inferences. We also studied the feature importance using shapley values based on game theories [54]. Mixing entropy, atomic size difference and melting temperature were identified as the top three most important features, largely consistent with the work of Yan et al [25]. More feature importance results can be found in Figure S4 of SI.

3.1.2 Moment tensor potentials

The trained MTP gave ∼5 meV/atom for the average absolute difference of energy and 0.058 eV/Å for the average absolute difference of atomic forces . To further validate the MTPs, we compared predicted lattice constants of single-element FCC crystals to values by DFT. We also compared the predicted surface energies of single-element FCC(111) facets with DFT. The comparison is summarized in Table. 1. One can see that MTP-predicted lattice constants are close to DFT calculations, with relative deviations around 1%. In terms of FCC(111) surface energies, although large deviations exist for elements Ni, Co and Al, the relative order of surface energy magnitude by MTP is in accordance with that by DFT.

We also compared the phase stability among various single-crystal structures, including FCC random alloys (FCC_A1), FCC L1$_2$ ordered structures and BCC B2 structures. This comparison was used to test the ability of MTPs to predict the most stable phase of Al$_x$(CrFeNiCo)$_{100-x}$ as a function Al compositions. Experimental observation and EAM-based calculations suggest that a
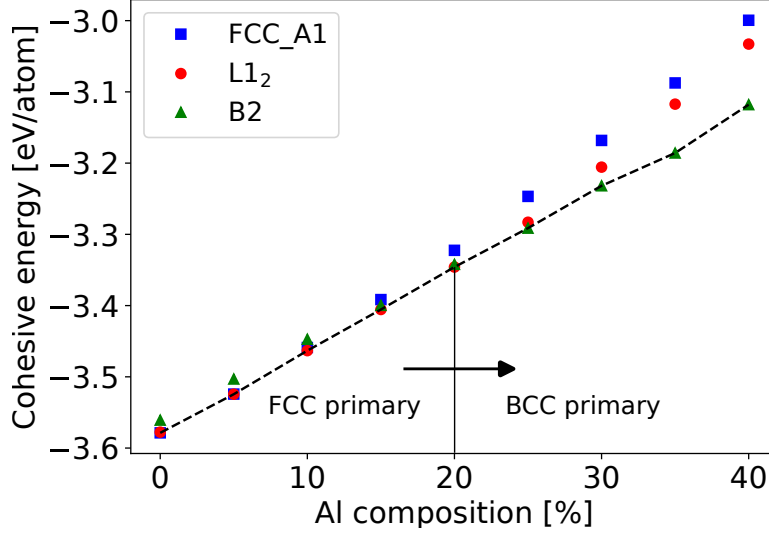
Figure 2: Cohesive energies of the FCC_A1, L1$_2$, and the ordered B2 phases for Al$_x$(CrFeCoNi)$_{100-x}$ as a function of Al compositions. The most stable phases at all Al compositions are connected with dashed lines to guide the eyes.

low Al composition favors FCC-type phases while B2 phases are thermodynamically more stable at higher Al compositions [7, 47]. We calculated the cohesive energies of L1$_2$ and B2 for Al compositions up to 40%, with all Al in one sublattice and the remaining four elements randomly distributed. The FCC_A1 structures were generated by randomly placing the atoms in a FCC lattice. Figure 2 shows that at low Al contents (0–10%), L1$_2$ and FCC_A1 are both more stable than B2 phases. When Al compositions increase (10–20%), the ordered L1$_2$ becomes the most stable phase. In comparison, larger Al compositions ($> 20\%$) favor the formation of ordered B2 phases, in good agreement with well-parameterized empirical potentials and experiments [7, 47]. The dashed line represents the most stable phases at each Al composition. One should note that the first-principles data used to train MTPs only consist of FCC structures. Despite not seeing any BCC structures, the MTPs accurately predicted the trends of phase stability that are consistent with experiments and first-principles data, indicating decent transferability of the MTPs.

3.2 Variation of three metrics as a function of Al and Cr compositions in AlCrFeCoNi

We examined the proposed machine learning framework by studying the three corrosion metrics for AlCrFeCoNi high-entropy alloys. This specific high-entropy system was used because of its superior corrosion performance and the availability of extensive experimental corrosion data, which were used to validate ML predictions [10, 55, 56]. The variations of three corrosion metrics are plotted in Figure 3 as a function of Al and Cr compositions in AlCrFeCoNi. Figure 3(a) shows results of single-phase formability. Although there is some noise in the training data as both multiple phases and single phase are found in the composition regions marked with black boxes, the random forest classifier accurately predicts 91% of all training data listed in Figure 3(a). Besides, one can see a decision boundary at around 10% Al composition to separate single-phase alloys and multiple-phase alloys. The decision boundary is mostly determined by Al compositions and

slightly associated with the Cr composition. An increased Cr composition will marginally shift the boundary to a lower Al composition. The trend of this decision boundary semi-quantitatively agrees with experimental data summarized by Wu et al [57], as indicated by the grey line in Figure 3(a). However, the prediction on the high Al composition region is confounded by the noisy training data, implying high prediction uncertainties in this region. If a single-phase structure is formed, we are also interested in which type of single phase structures will be formed since experiments found FCC crystals to be more resistant to pitting corrosion than BCC crystals [10, 56]. We identified the type of single phase to form for a given composition by comparing the cohesive energies of $L1_2$ FCC and B2 BCC phases following a similar procedure describe in the Section ML prediction accuracy and transferability. The variation of single-phase structures across different Al and Cr compositions are presented in Figure S5. Figure 3(a) and Figure S5 jointly show that FCC phases form at low Al and Cr compositions while BCC phases are more likely to form at high Al and Cr compositions.

Figure. 3(b) shows PBR_{Cr} for different Al and Cr compositions. Likewise, a major dependence on Al compositions and a minor dependence on Cr compositions are identified. PBR_{Cr} values in the entire composition space studied have a lower bound of 2.00 and a upper bound of 2.18, both of which are close to the PBR_{Cr} of pure Cr (2.04). According to the analysis by Bernstein [58] and Huntz et al. [59], the oxide stresses are related to PBR by $\epsilon = \omega[(PBR)^{1/3} - 1]$ where ω is a correction factor around 0.18. Therefore, the oxide stresses across all Al and Cr compositions studied only show a negligible difference of around 0.5%. In contrast, the surface energies exhibit more significant variations over compositions, ranging from 1.92 to 2.24 J/m^2. Using an atomic density of 1×10^{19} atoms/m^2 and a transition coefficient α of 1/2, electrochemical dissolution rates given by Eq. 2 vary by 50 folds. High surface energies are concentrated at the regions with high Al and Cr compositions, while low surface energies are found with Cr contents around 18% and with either low or high Al contents. To understand surface energy dependency on Al and Cr, we studied the surface segregation of Al and Cr for each composition, and the results are depicted in Figure S6. It is thus inferred that the low surface energies at the right-bottom region of Figure 3(c) originate from Al segregation and Cr depletion, probably because a Al FCC(111) surface has a much lower surface energy (0.77 J/m^2) compared to a Cr FCC(111) surface (2.61 J/m^2), as shown in Table 1. The Cr depletion on the surface lends itself difficult to formation of Cr_2O_3 passive films. Thus, highly corrosion-resistant AlCrFeCoNi alloys can potentially be found with low Al contents and around 18% Cr contents because the alloy with these compositions tend to form single-phase alloys and to exhibit low surface energies. The identified Al composition is consistent with experimental measurement [10, 31, 56].

4   Conclusion and outlook

A machine learning framework was proposed and developed to accelerate the discovery of corrosion-resistant high-entropy alloys. We demonstrated that the proposed framework can provide an accurate evaluation of relative corrosion resistance for a wide range of compositions for high-entropy alloys. The physics-informed framework consists of two machine learning approaches. One approach uses experimental data to train random forest classifier for predictions of single phase formability. The other approach uses first-principles data to develop robust machine learning potentials, allowing for fast downstream simulations to obtain corrosion metrics such as Pilling-Bedworth ratio
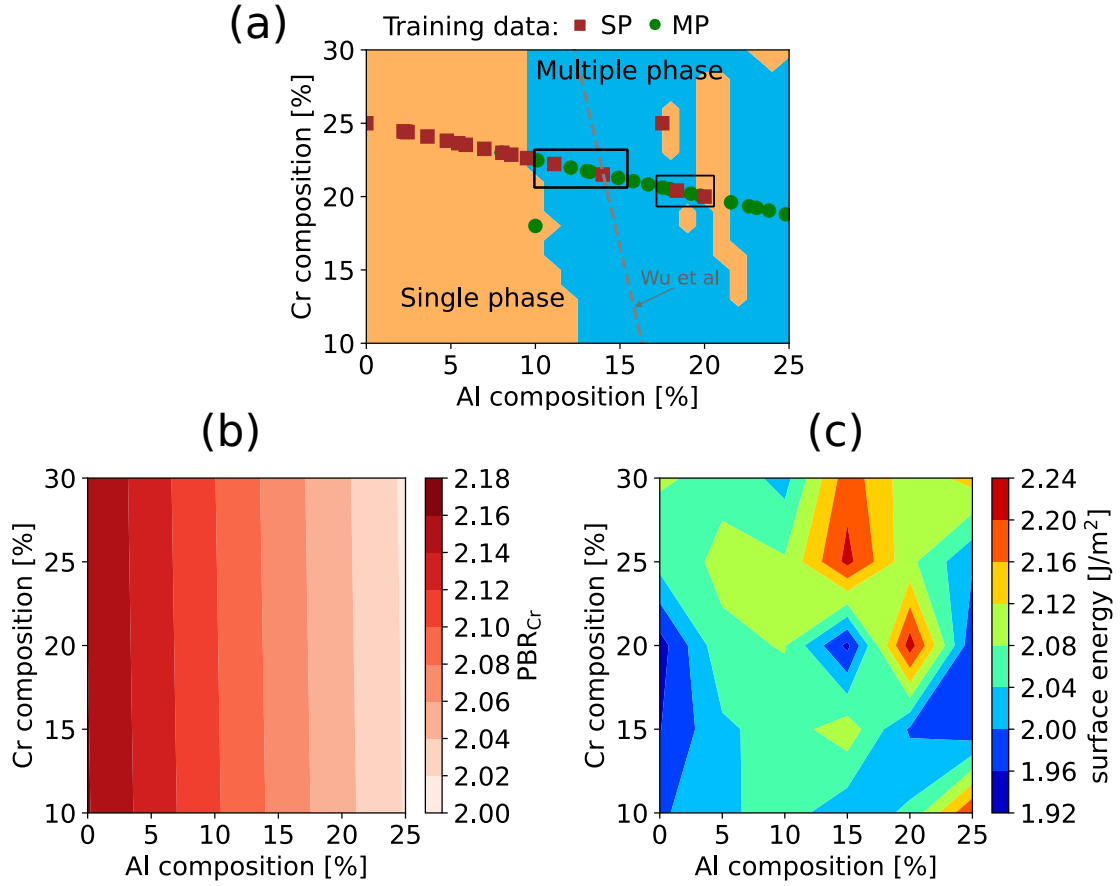
Figure 3: Single phase formability (a), Pilling-Bedworth ratios for oxidation of Cr (b) and FCC(111) surface energies (c) as a function of Al and Cr compositions in $Al_xCr_y(FeCoNi)_{100-x-y}$. The training data involving AlCrFeCoNi high-entropy alloys are included as scatter points in (a). Red squares and green circles in (a) represent single phase and multiple phase data, respectively. The grey dashed line in (a) is roughly the decision boundary by Wu et al [57]. The regions where multi phases and single phase are almost overlapped are marked with black boxes in (a).

and surface energy. Current computational methods to understand corrosion performance of alloys mostly use pure statistical fitting or first-principles calculations. Unlike statistical fitting, the random forest classifier encodes meaningful physical knowledge into the feature engineering process. In comparison with first-principles calculations, the machine learning potentials can significantly mitigate the computational overhead of massive first-principles calculations. This framework was tested on a specific class of high-entropy alloys AlCrFeCoNi. The AlCrFeCoNi compositions were sampled by varying the Al and Cr compositions while enforcing the remaining Fe, Co and Ni compositions to be almost identical. The three corrosion metrics were evaluated on those sampled compositions, based on which the desired compositions for corrosion protection were identified. We found that low Al compositions and around 18% Cr compositions tend to form corrosion-resistant alloys, in satisfactory agreement with experimental observations. Although additional corrosion descriptors, such as cohesive energy, and adsorption energy of oxygen and chloride, may be needed to provide a more comprehensive description of corrosion performance, the three simple corrosion metrics used in this work have proved to be effective in narrowing down the composition space for further selection.

Our scheme is not limited to AlCrFeCoNi high-entropy alloys and corrosion properties. The methodology can be easily adapted for other material applications where the relationship of chemical compositions with properties is sought after and where ML accelerated molecular simulations are indispensable for high-throughput screening of material candidates. For instance, ductility of alloys can be evaluated by stacking fault energies which can be calculated by using MLPs, and hardness can be estimated using machine learning regression on experimental dataset [60, 61]. One should note that most state-of-the-art machine learning potentials use element-specific features, which limit the transferability of MLPs. In other words, MLPs trained on certain elements cannot be applied to elements not existing in the training data. Moreover, a large amount of training structures are required to build reliable ML models for high-entropy systems. Developing a robust element-agnostic featurization method, and reducing numbers of representative images and features are promising future directions. Element-agnostic featurization methods are just emerging in recent years and needs further development. For example, there are methods using multipole expansions of the electron density around atoms [62] or graph representation of materials [63]. Current image and feature selection methods use linear correlations in the feature space [64]. More advanced methods may require understand the complex non-linear mapping between features and outputs (e.g. energy and forces).

Declaration of competing interest

The authors declare that they have no known competing financial interests or personal relationships that could have appeared to influence the work reported in this paper.

Acknowledgments

Supporting information

Standard enthalpy of formation for oxides of certain metals, Computational settings of DFT calculations, Details of moment tensor potential (MTP), Random forest classifier for single phase formability, Fast sampling of configurations using the embedded atom method (EAM), First-principles data for MTP, MTP-enabled simulations for corrosion metrics, and Supporting results are included in the supporting information.

Data and code availability

Code and data to reproduce the findings can be found on github: https://github.com/cengc13/ml-hea-corrosion-code-data.

References

[1] Cantor, B.; Chang, I.T.H.; Knight, P.; Vincent, A.J.B. Microstructural development in equiatomic multicomponent alloys. *Materials Science and Engineering: A* **2004**; 375-377, 213–218.

[2] Yeh, J.W.; Chen, S.K.; Lin, S.J.; Gan, J.Y.; Chin, T.S.; Shun, T.T.; Tsau, C.H.; Chang, S.Y. Nanostructured High-Entropy Alloys with Multiple Principal Elements: Novel Alloy Design Concepts and Outcomes. *Advanced Engineering Materials* **2004**; 6, 299–303.

[3] Gludovatz, B.; Hohenwarter, A.; Catoor, D.; Chang, E.H.; George, E.P.; Ritchie, R.O. A fracture-resistant high-entropy alloy for cryogenic applications. *Science* **2014**; 345, 1153–1158.

[4] Yang, T.; Zhao, Y.L.; Tong, Y.; Jiao, Z.B.; Wei, J.; Cai, J.X.; Han, X.D.; Chen, D.; Hu, A.; Kai, J.J.; Lu, K.; Liu, Y.; Liu, C.T. Multicomponent intermetallic nanoparticles and superb mechanical behaviors of complex alloys. *Science* **2018**; 362, 933–937.

[5] Li, Z.; Pradeep, K.G.; Deng, Y.; Raabe, D.; Tasan, C.C. Metastable high-entropy dual-phase alloys overcome the strength–ductility trade-off. *Nature* **2016**; 534, 227–230.

[6] Ding, Z.Y.; Cao, B.X.; Luan, J.H.; Jiao, Z.B. Synergistic effects of Al and Ti on the oxidation behaviour and mechanical properties of L12-strengthened FeCoCrNi high-entropy alloys. *Corrosion Science* **2021**; 184, 109365.

[7] Wang, W.R.; Wang, W.L.; Wang, S.C.; Tsai, Y.C.; Lai, C.H.; Yeh, J.W. Effects of Al addition on the microstructure and mechanical property of AlxCoCrFeNi high-entropy alloys. *Intermetallics* **2012**; 26, 44–51.

[8] Kumar, N.A.P.K.; Li, C.; Leonard, K.J.; Bei, H.; Zinkle, S.J. Microstructural stability and mechanical behavior of FeNiMnCr high entropy alloy under ion irradiation. *Acta Materialia* **2016**; 113, 230–244.

[9] Lu, Y.; Huang, H.; Gao, X.; Ren, C.; Gao, J.; Zhang, H.; Zheng, S.; Jin, Q.; Zhao, Y.; Lu, C.; Wang, T.; Li, T. A promising new class of irradiation tolerant materials: Ti2ZrHfV0.5Mo0.2 high-entropy alloy. *Journal of Materials Science & Technology* **2019**; 35, 369–373.

[10] Shi, Y.; Collins, L.; Feng, R.; Zhang, C.; Balke, N.; Liaw, P.K.; Yang, B. Homogenization of AlxCoCrFeNi high-entropy alloys with improved corrosion resistance. *Corrosion Science* **2018**; 133, 120–131.

[11] Qiu, Y.; Gibson, M.A.; Fraser, H.L.; Birbilis, N. Corrosion characteristics of high entropy alloys. *Materials Science and Technology* **2015**; 31, 1235–1243.

[12] Fu, Y.; Li, J.; Luo, H.; Du, C.; Li, X. Recent advances on environmental corrosion behavior and mechanism of high-entropy alloys. *Journal of Materials Science & Technology* **2021**; 80, 217–233.

[13] Steurer, W. Single-phase high-entropy alloys – A critical update. *Materials Characterization* **2020**; 162, 110179.

[14] Zhao, Y.J.; Qiao, J.W.; Ma, S.G.; Gao, M.C.; Yang, H.J.; Chen, M.W.; Zhang, Y. A hexagonal close-packed high-entropy alloy: The effect of entropy. *Materials & Design* **2016**; 96, 10–15.

[15] Taylor, C.D.; Lu, P.; Saal, J.; Frankel, G.S.; Scully, J.R. Integrated computational materials engineering of corrosion resistant alloys. *npj Mater Degrad* **2018**; 2, 1–10.

[16] Nyby, C.; Guo, X.; Saal, J.E.; Chien, S.C.; Gerard, A.Y.; Ke, H.; Li, T.; Lu, P.; Oberdorfer, C.; Sahu, S.; Li, S.; Taylor, C.D.; Windl, W.; Scully, J.R.; Frankel, G.S. Electrochemical metrics for corrosion resistant alloys. *Sci Data* **2021**; 8, 58.

[17] Ansari, T.Q.; Huang, H.; Shi, S.Q. Phase field modeling for the morphological and microstructural evolution of metallic materials under environmental attack. *npj Comput Mater* **2021**; 7, 1–21.

[18] Diao, Y.; Yan, L.; Gao, K. Improvement of the machine learning-based corrosion rate prediction model through the optimization of input features. *Materials & Design* **2021**; 198, 109326.

[19] Roy, A.; Taufique, M.F.N.; Khakurel, H.; Devanathan, R.; Johnson, D.D.; Balasubramanian, G. Machine-learning-guided descriptor selection for predicting corrosion resistance in multi-principal element alloys. *npj Mater Degrad* **2022**; 6, 1–10.

[20] Ke, H.; Taylor, C.D. Density Functional Theory: An Essential Partner in the Integrated Computational Materials Engineering Approach to Corrosion. *Corrosion* **2019**; 75, 708–726.

[21] Chen, Z.; Jafarzadeh, S.; Zhao, J.; Bobaru, F. A coupled mechano-chemical peridynamic model for pit-to-crack transition in stress-corrosion cracking. *Journal of the Mechanics and Physics of Solids* **2021**; 146, 104203.

[22] Li, T.; Wu, J.; Frankel, G.S. Localized corrosion: Passive film breakdown vs. Pit growth stability, Part VI: Pit dissolution kinetics of different alloys and a model for pitting and repassivation potentials. *Corrosion Science* **2021**; 182, 109277.

[23] Ren, J.; Zhang, Y.; Zhao, D.; Chen, Y.; Guan, S.; Liu, Y.; Liu, L.; Peng, S.; Kong, F.; Poplawsky, J.D.; Gao, G.; Voisin, T.; An, K.; Wang, Y.M.; Xie, K.Y.; Zhu, T.; Chen, W. Strong yet ductile nanolamellar high-entropy alloys by additive manufacturing. *Nature* **2022**; 608, 62–68.

[24] Mao, H.; Chen, H.L.; Chen, Q. TCHEA1: A Thermodynamic Database Not Limited for "High Entropy" Alloys. *J. Phase Equilib. Diffus.* **2017**; 38, 353–368.

[25] Yan, Y.; Lu, D.; Wang, K. Accelerated discovery of single-phase refractory high entropy alloys assisted by machine learning. *Computational Materials Science* **2021**; 199, 110723.

[26] Zeng, C.; Ling, Y.; Bai, Y.; Zhang, R.; Dai, X.; Chen, Y. Hydrogen permeation characteristic of nanoscale passive films formed on different zirconium alloys. *International Journal of Hydrogen Energy* **2016**; 41, 7676–7690.

[27] Zeng, C.; Bai, Y.; Ling, Y.; Xin, Z.; Liang, H.; Deng, X. Hydrogen interaction characteristic of nanoscale oxide films grown on iron–nickel based stainless steel by selective thermal oxidation. *International Journal of Hydrogen Energy* **2017**; 42, 20910–20921.

[28] Xu, C.; Gao, W. Pilling-Bedworth ratio for oxidation of alloys. *Materials Research Innovations* **2000**; 3, 231–235.

[29] Sabioni, A.C.S.; Huntz, A.M.; Silva, F.; Jomard, F. Diffusion of iron in Cr2O3: polycrystals and thin films. *Materials Science and Engineering: A* **2005**; 392, 254–261.

[30] Tsai, K.Y.; Tsai, M.H.; Yeh, J.W. Sluggish diffusion in Co–Cr–Fe–Mn–Ni high-entropy alloys. *Acta Materialia* **2013**; 61, 4887–4897.

[31] Shi, Y.; Yang, B.; Rack, P.D.; Guo, S.; Liaw, P.K.; Zhao, Y. High-throughput synthesis and corrosion behavior of sputter-deposited nanocrystalline Alx(CoCrFeNi)100-x combinatorial high-entropy alloys. *Materials & Design* **2020**; 195, 109018.

[32] Song, G.L.; Mishra, R.; Xu, Z. Crystallographic orientation and electrochemical activity of AZ31 Mg alloy. *Electrochemistry Communications* **2010**; 12, 1009–1012.

[33] Ramachandran, R.; Nosonovsky, M. Coupling of surface energy with electric potential makes superhydrophobic surfaces corrosion-resistant. *Phys. Chem. Chem. Phys.* **2015**; 17, 24988–24997.

[34] Bowler, D.R.; Miyazaki, T. $\mathcal{O}(N)$ methods in electronic structure calculations. *Reports on Progress in Physics* **2012**; 75, 036503.

[35] Kohn, W. Density Functional and Density Matrix Method Scaling Linearly with the Number of Atoms. *Physical Review Letters* **1996**; 76, 3168–3171.

[36] Behler, J.; Parrinello, M. Generalized Neural-Network Representation of High-Dimensional Potential-Energy Surfaces. *Physical Review Letters* **2007**; 98, 146401.

[37] Zeng, C.; Chen, X.; Peterson, A.A. A nearsighted force-training approach to systematically generate training data for the machine learning of large atomic structures. *The Journal of Chemical Physics* **2022**; 156, 064104.

[38] Xie, T.; Grossman, J.C. Crystal Graph Convolutional Neural Networks for an Accurate and Interpretable Prediction of Material Properties. *Physical Review Letters* **2018**; 120, 145301. Publisher: American Physical Society.

[39] Bartók, A.P.; Payne, M.C.; Kondor, R.; Csányi, G. Gaussian Approximation Potentials: the accuracy of quantum mechanics, without the electrons. *Physical Review Letters* **2010**; 104, 136403.

[40] Rupp, M.; Tkatchenko, A.; Müller, K.R.; von Lilienfeld, O.A. Fast and Accurate Modeling of Molecular Atomization Energies with Machine Learning. *Physical Review Letters* **2012**; 108, 058301.

[41] Batzner, S.; Musaelian, A.; Sun, L.; Geiger, M.; Mailoa, J.P.; Kornbluth, M.; Molinari, N.; Smidt, T.E.; Kozinsky, B. E(3)-equivariant graph neural networks for data-efficient and accurate interatomic potentials. *Nat Commun* **2022**; 13, 2453.

[42] Zeng, C.; Sahoo, S.J.; Medford, A.J.; Peterson, A.A. The phase stability of large-size nanoparticle alloy catalysts at ab initio quality using a nearsighted force-training approach **2023**.

[43] Behler, J.; Csányi, G. Machine learning potentials for extended systems: a perspective. *Eur. Phys. J. B* **2021**; 94, 142.

[44] Zuo, Y.; Chen, C.; Li, X.; Deng, Z.; Chen, Y.; Behler, J.; Csányi, G.; Shapeev, A.V.; Thompson, A.P.; Wood, M.A.; Ong, S.P. Performance and Cost Assessment of Machine Learning Interatomic Potentials. *J. Phys. Chem. A* **2020**; 124, 731–745.

[45] Shapeev, A.V. Moment Tensor Potentials: A Class of Systematically Improvable Interatomic Potentials. *Multiscale Model. Simul.* **2016**; 14, 1153–1173.

[46] Novikov, I.S.; Gubaev, K.; Podryabinkin, E.V.; Shapeev, A.V. The MLIP package: moment tensor potentials with MPI and active learning. *Mach. Learn.: Sci. Technol.* **2020**; 2, 025002. Publisher: IOP Publishing.

[47] Farkas, D.; Caro, A. Model interatomic potentials for Fe–Ni–Cr–Co–Al high-entropy alloys. *Journal of Materials Research* **2020**; 35, 3031–3040.

[48] Dohn, A.O.; Jónsson, E.Ö.; Levi, G.; Mortensen, J.J.; Lopez-Acevedo, O.; Thygesen, K.S.; Jacobsen, K.W.; Ulstrup, J.; Henriksen, N.E.; Møller, K.B.; Jónsson, H. Grid-Based Projector Augmented Wave (GPAW) Implementation of Quantum Mechanics/Molecular Mechanics (QM/MM) Electrostatic Embedding and Application to a Solvated Diplatinum Complex. *Journal of Chemical Theory and Computation* **2017**; 13, 6010–6022.

[49] Zunger, A.; Wei, S.H.; Ferreira, L.G.; Bernard, J.E. Special quasirandom structures. *Phys. Rev. Lett.* **1990**; 65, 353–356.

[50] van de Walle, A.; Tiwary, P.; de Jong, M.; Olmsted, D.L.; Asta, M.; Dick, A.; Shin, D.; Wang, Y.; Chen, L.Q.; Liu, Z.K. Efficient stochastic generation of special quasirandom structures. *Calphad* **2013**; 42, 13–18.

[51] Hjorth Larsen, A.; Jørgen Mortensen, J.; Blomqvist, J.; Castelli, I.E.; Christensen, R.; Dułak, M.; Friis, J.; Groves, M.N.; Hammer, B.; Hargus, C.; Hermes, E.D.; Jennings, P.C.; Bjerre Jensen, P.; Kermode, J.; Kitchin, J.R.; Leonhard Kolsbjerg, E.; Kubal, J.; Kaasbjerg, K.; Lysgaard, S.; Bergmann Maronsson, J.; Maxson, T.; Olsen, T.; Pastewka, L.; Peterson, A.; Rostgaard, C.; Schiøtz, J.; Schütt, O.; Strange, M.; Thygesen, K.S.; Vegge, T.; Vilhelmsen, L.; Walter, M.; Zeng, Z.; Jacobsen, K.W. The atomic simulation environment—a Python library for working with atoms. *Journal of Physics: Condensed Matter* **2017**; 29, 273002.

[52] Thompson, A.P.; Aktulga, H.M.; Berger, R.; Bolintineanu, D.S.; Brown, W.M.; Crozier, P.S.; in 't Veld, P.J.; Kohlmeyer, A.; Moore, S.G.; Nguyen, T.D.; Shan, R.; Stevens, M.J.; Tranchida, J.; Trott, C.; Plimpton, S.J. LAMMPS - a flexible simulation tool for particle-based materials modeling at the atomic, meso, and continuum scales. *Computer Physics Communications* **2022**; 271, 108171.

[53] Sieradzki, K.; Newman, R.C. A Percolation Model for Passivation in Stainless Steels. *J. Electrochem. Soc.* **1986**; 133, 1979.

[54] Merrick, L.; Taly, A. The Explanation Game: Explaining Machine Learning Models Using Shapley Values. In A. Holzinger; P. Kieseberg; A.M. Tjoa; E. Weippl, eds., *Machine Learning and Knowledge Extraction*, Lecture Notes in Computer Science. Springer International Publishing, Cham. ISBN 978-3-030-57321-8, pp. 17–38.

[55] Shi, H.; Jianu, A.; Fetzer, R.; Szabó, D.V.; Schlabach, S.; Weisenburger, A.; Tang, C.; Heinzel, A.; Lang, F.; Müller, G. Compatibility and microstructure evolution of Al-Cr-Fe-Ni high entropy model alloys exposed to oxygen-containing molten lead. *Corrosion Science* **2021**; 189, 109593.

[56] Shi, Z.J.; Wang, Z.B.; Wang, X.D.; Zhang, S.; Zheng, Y.G. Effect of thermally induced B2 phase on the corrosion behavior of an Al0.3CoCrFeNi high entropy alloy. *Journal of Alloys and Compounds* **2022**; 903, 163886.

[57] Wu, Q.; Wang, Z.; Hu, X.; Zheng, T.; Yang, Z.; He, F.; Li, J.; Wang, J. Uncovering the eutectics design by machine learning in the Al–Co–Cr–Fe–Ni high entropy system. *Acta Materialia* **2020**; 182, 278–286.

[58] Bernstein, H.L. A model for the oxide growth stress and its effect on the creep of metals. *Metall Trans A* **1987**; 18, 975–986.

[59] Huntz, A.M. Stresses in NiO, Cr2O3 and Al2O3 oxide scales. *Materials Science and Engineering: A* **1995**; 201, 211–228.

[60] Hu, Y.J.; Sundar, A.; Ogata, S.; Qi, L. Screening of generalized stacking fault energies, surface energies and intrinsic ductile potency of refractory multicomponent alloys. *Acta Materialia* **2021**; 210, 116800.

[61] Yang, C.; Ren, C.; Jia, Y.; Wang, G.; Li, M.; Lu, W. A machine learning-based alloy design system to facilitate the rational design of high entropy alloys with enhanced hardness. *Acta Materialia* **2022**; 222, 117431.

[62] Lei, X.; Medford, A.J. A Universal Framework for Featurization of Atomistic Systems. *J. Phys. Chem. Lett.* **2022**; 13, 7911–7919.

[63] Chen, C.; Ong, S.P. A universal graph deep learning interatomic potential for the periodic table. *Nat Comput Sci* **2022**; 2, 718–728.

[64] Imbalzano, G.; Anelli, A.; Giofré, D.; Klees, S.; Behler, J.; Ceriotti, M. Automatic selection of atomic fingerprints and reference configurations for machine-learning potentials. *The Journal of Chemical Physics* **2018**; 148, 241730.